

# On the Origin of Flux Ratio Anomaly in Quadruple Lens Systems

Kaiki Taro Inoue<sup>1\*</sup>

<sup>1</sup>*Faculty of Science and Engineering, Kindai University, Higashi-Osaka, 577-8502, Japan*

8 March 2018

## ABSTRACT

We explore the origin of flux ratio anomaly in quadruple lens systems. Using a semi-analytic method based on  $N$ -body simulations, we estimate the effect of possible magnification perturbation caused by subhaloes with a mass scale of  $\lesssim 10^9 h^{-1} M_{\odot}$  in lensing galaxy haloes. Taking into account astrometric shifts, assuming that the primary lens is described by a singular isothermal ellipsoid, the expected change to the flux ratios per a multiply lensed image is just a few percent and the mean of the expected convergence perturbation at the effective Einstein radius of the lensing galaxy halo is  $\langle \delta\kappa_{\text{sub}} \rangle = 0.003$ , corresponding to the mean of the ratio of a projected dark matter mass fraction in subhaloes at the effective Einstein radius  $\langle f_{\text{sub}} \rangle = 0.006$ . In contrast, the expected change to the flux ratio caused by line-of-sight structures is typically  $\sim 10$  percent and the mean of the convergence perturbation is  $\langle |\delta\kappa_{\text{los}}| \rangle = 0.008$ , corresponding to  $\langle f_{\text{los}} \rangle = 0.017$ . The contribution of magnification perturbation caused by subhaloes is  $\sim 40$  percent of the total at a source redshift  $z_S = 0.7$  and decreases monotonically in  $z_S$  to  $\sim 20$  percent at  $z_S = 3.6$ . Assuming statistical isotropy, the convergence perturbation estimated from observed 11 quadruple lens systems has a positive correlation with the source redshift  $z_S$ , which is much stronger than that with the lens redshift  $z_L$ . This feature also supports an idea that the flux ratio anomaly is caused mainly by line-of-sight structures rather than subhaloes. We also discuss about a possible imprint of line-of-sight structures in demagnification of minimum images due to locally underdense structures in the line of sight.

**Key words:** galaxies: formation - cosmology: theory - gravitational lensing - dark matter.

## 1 INTRODUCTION

It has been known that some quadruply lensed quasars show anomalies in the observed flux ratios of lensed images provided that the gravitational potential of the lensing galaxy halo is sufficiently smooth. Such a discrepancy is called the “anomalous flux ratio” and has been considered as an imprint of cold dark matter (CDM) subhaloes with a mass of  $\sim 10^{8-9} M_{\odot}$  in the parent galaxy haloes (Mao & Schneider 1998; Metcalf & Madau 2001; Chiba 2002; Dalal & Kochanek 2002; Keeton et al. 2003; Inoue & Chiba 2003; Kochanek & Dalal 2004; Metcalf et al. 2004; Chiba et al. 2005; Sugai et al. 2007; McKean et al. 2007; More et al. 2009; Minezaki et al. 2009; Xu et al. 2009, 2010; Fadely & Keeton 2012; MacLeod et al. 2013).

However, intergalactic haloes in the line of sight can act as perturbers as well (Chen et al. 2003; Metcalf 2005; Xu et al. 2012). Indeed, taking into account astrometric

shifts, recent studies have found that the observed anomalous flux ratios can be explained solely by line-of-sight structures with a surface density  $\sim 10^{7-8} h^{-1} M_{\odot}/\text{arcsec}^2$  (Inoue & Takahashi 2012; Takahashi & Inoue 2014; Inoue et al. 2015, 2016) without taking into account subhaloes in the lensing galaxies. Moreover, using the cusp and fold caustic relations expressed in statistics  $R_{\text{cusp}}$  and  $R_{\text{fold}}$ , Xu et al. (2015) found that the perturbation caused by subhaloes is not sufficient for explaining the observed anomalies.

In order to model quadruple lens systems, one must take into account other massive objects that may significantly affect the flux ratios (McKean et al. 2007; More et al. 2009). Moreover, disk components can also significantly perturb the flux ratios (Hsueh et al. 2016). Thus, it is sometimes difficult to make constraints using the cusp and fold caustic relations because they hold only in lenses with a smooth potential and small angles between two bright lensed images.

In this paper, we investigate the origin of flux ratio anomaly in 11 quadruple lens systems including radio and

\* E-mail: kinoue@phys.kindai.ac.jp

mid-infrared (MIR) fluxes. We do not use the “traditional” statistics  $R_{\text{cusp}}$  and  $R_{\text{fold}}$  in the literature. The reasons are: 1) the lens systems can have more complex structures such as a secondary and a third lens. 2) the cusp and fold caustic relations do not exactly hold because the angle between two images in a triplet or a double is not necessarily small. 3) the magnification bias in the selection of lens candidates can significantly affect the statistics. We also use the information of possible astrometric shifts, which was often ignored in the literature (see, however, [Chen et al. \(2007\)](#); [Sluse et al. \(2012\)](#)). Furthermore, we pay attention to the correlation between the perturbation to the fluxes and the redshifts of the primary lenses and the source, which would shed a new light on the origin of the flux ratio anomaly.

In section 2, we estimate the perturbation effects caused by subhaloes in lensing galaxies using a semi-analytic mass function of subhaloes. In section 3, we briefly describe our method for calculating the perturbation effects caused by line-of-sight structures. In section 4, we briefly describe the 11 quadruple lenses. In section 5, we explain the adopted lens model of an unperturbed system. In section 6, we explain our method using a statistic “ $\eta$ ” for fitting the model to the data. In section 7, we show our result for the magnification and convergence perturbations and their correlations with the lens and source redshifts. In section 8, we briefly discuss about a new type of anomaly that can be used for distinguishing the origin of the perturbation.

In what follows, we assume a cosmology with a matter density  $\Omega_{m,0} = 0.3134$ , a baryon density  $\Omega_{b,0} = 0.0487$ , a cosmological constant  $\Omega_{\Lambda,0} = 0.6866$ , a Hubble constant  $H_0 = 67.3 \text{ km/s/Mpc}$ , a spectral index  $n_s = 0.9603$ , and the root-mean-square (rms) amplitude of matter fluctuations at  $8h^{-1} \text{ Mpc}$ ,  $\sigma_8 = 0.8421$ , which are obtained from the observed CMB (Planck+WMAP polarization; [Planck Collaboration et al. \(2014\)](#)).  $m$  and  $r$  refer to the mass and radius of a subhalo, and  $M$  and  $R$  refer to the mass of the host and the radial location within a host. The virial mass  $M_{200}$  is the mass inside the virial radius  $R_{200}$  inside which the average matter density equals 200 times the critical density of the universe.

## 2 SUBSTRUCTURE LENSING

In order to estimate the magnification perturbation due to subhaloes in a lensing galaxy halo, we need to calculate the mass function of subhaloes.

At a proper distance  $R$  from the centre of a host halo, the number density of subhaloes  $n$  per a logarithmic interval of the mass  $m_{\text{in}}$  of subhaloes at the infall is well approximated by

$$\frac{dn(m_{\text{in}}, R)}{d \ln m_{\text{in}}} \propto m_{\text{in}}^{-\alpha} \rho(R), \quad (1)$$

where  $\rho(R)$  is the density of the host halo at  $R$  and  $\alpha \sim 0.9$  ([van den Bosch et al. 2005](#))<sup>1</sup>.

However, after infalling, the masses of subhaloes are stripped off by the tidal force of the host halo, and some of them are completely disrupted. Therefore, the mass  $m$

of a subhalo at the time of deflection of photons can be significantly reduced at the position of lensed images.

Assuming that subhaloes have a density profile similar to that of an singular isothermal sphere (SIS), the bound fraction  $\mu = m/m_{\text{in}}$  of subhaloes at  $R$  can be approximated as

$$\mu(R) \propto R^\beta, \quad (2)$$

where  $\beta \sim 1$  if the kinetic energy of subhaloes is negligible. In real setting, one must also consider the kinetic energy of subhaloes at the time of infall and the change of tidal stripping that depend both on the orbit and the background gravitational field. If tidal stripping of each subhalo can be treated as an uncorrelated random process, one may approximate the set of bound fraction  $\mu$  for each subhalo as random variables. Assuming that  $\mu$  is written in terms of a polynomial and obeys a log-normal distribution and the spatial distribution with a given infall mass traces the mass density profile, based on two sets of high-resolution cosmological  $N$ -body simulations; the Aquarius ([Springel et al. 2008](#)) and Phoenix ([Gao et al. 2012](#)) simulation suites, [Han et al. \(2016\)](#) obtained a subhalo mass function for a host halo with  $R_{200}$  and  $M_{200}$ ,

$$\frac{dn(m, R)}{d \ln m} = A_{\text{acc}} B f_s e^{\sigma^2 \alpha^2 / 2} \left[ \frac{m}{m_0 \bar{\mu}(R)} \right]^{-\alpha} \frac{\rho(R)}{m_0}, \quad (3)$$

where the mean bound fraction is

$$\bar{\mu}(R) = \mu_* \left( \frac{R}{R_{200}} \right)^\beta \quad (4)$$

and

$$\begin{aligned} \mu_* &= 0.5 (M_{200}/m_0)^{-0.03}, \quad \alpha = 0.95, \\ \beta &= 1.7 (M_{200}/m_0)^{-0.04}, \quad A_{\text{acc}} = 0.1 (M_{200}/m_0)^{-0.02} \\ f_s &= 0.55, \quad m_0 = 10^{10} h^{-1} M_\odot. \end{aligned} \quad (5)$$

Let us assume that a parent halo that hosts a primary lensing galaxy has an NFW profile with a concentration parameter  $C$  and a critical density  $\rho_{\text{crit}}$  at a redshift  $z$ ,

$$\rho^{\text{NFW}}(R) = \frac{\delta_c(C) \rho_{\text{crit}}(z)}{(R/R_{-2})(1 + R/R_{-2})^2}, \quad (6)$$

where

$$R_{-2} = R_{200}/C, \quad \delta_c(C) = \frac{200}{3} \frac{C^3}{\ln[1 + C] - C/(1 + C)}. \quad (7)$$

Integrating equation (3) over the line of sight, we obtain the mass function projected onto the lens plane as a function of  $m$  and the projected proper distance  $R_{2D}$  to the host halo center in the lens plane as

$$\begin{aligned} \frac{dn_s(m, R_{2D})}{d \ln m} &= A_{\text{acc}} B f_s e^{\sigma^2 \alpha^2 / 2} \left[ \frac{m}{m_0} \right]^{-\alpha} \frac{\delta_c(C) \rho_{\text{crit}}(z)}{m_0} \\ &\times K[R_{2D}, R_{200}/C, \gamma], \end{aligned} \quad (8)$$

<sup>1</sup> In the literature, the other definition  $\tilde{\alpha} = \alpha + 1$  is sometimes used.

where  $n_s$  is the surface number density,  $\gamma = \alpha\beta$  and

$$\begin{aligned}
 & K[R_{2D}, R_{200}/C, \gamma] \\
 &= 2^{2-\gamma} \mu_*^\alpha \frac{R_{200}^{-\gamma} R_{2D}^{-3+\gamma} R_{-2}^3}{\Gamma[3-\alpha\beta](R_{2D}^2 - R_{-2}^2)} \\
 &\times \left[ (\Gamma[3/2 - \gamma/2])^2 R_{-2} \left( (-2 + \gamma) R_{2D}^2 - (R_{-2}^2 + \gamma(R_{2D}^2 \right. \right. \\
 &\left. \left. - R_{-2}^2)) {}_2F_1 \left[ 1, \frac{3-\gamma}{2}, 2 - \frac{\gamma}{2}, \frac{R_{-2}^2}{R_{2D}^2} \right] \right) \\
 &+ \Gamma[1 - \gamma/2] \Gamma[2 - \gamma/2] R_{2D} (R_{2D}^2 - R_{-2}^2) \\
 &\times {}_3F_2 \left[ 1, \frac{3}{2}, \frac{1-\gamma}{2}; \frac{1}{2}, \frac{3-\gamma}{2}; \frac{R_{-2}^2}{R_{2D}^2} \right] \right]. \quad (9)
 \end{aligned}$$

Equations (8) and (9) give the surface mass density  $\Sigma_s$  and the surface number density  $n_s$  of subhaloes at a distance  $R_{2D}$  in an NFW halo,

$$\Sigma_s(R_{2D}) = \int_{m_{min}}^{m_{max}} \frac{dn_s(m, R_{2D})}{d \ln m} dm, \quad (10)$$

$$n_s(R_{2D}) = \int_{m_{min}}^{m_{max}} \frac{dn_s(m, R_{2D})}{d \ln m} d \ln m, \quad (11)$$

where  $m_{min}$  and  $m_{max}$  are the minimum and the maximum mass of the subhaloes. Note that the obtained sub-

halo surface number densities are consistent with those in (Xu et al. 2015) in which 500 random projections are used per halo in the Aquarius and Phoenix simulations. As we shall show in section 7, the effective Einstein radius is  $R_E \sim 0.01 R_{200}$ . As shown in Fig. 1, at projected proper distances  $R_{2D} \lesssim 0.03 R_{200}$ , for  $M_{200} = 10^{12-13} h^{-1} M_\odot$ , the surface mass density is nearly constant due to tidal disruption. Since for  $R_{2D} < R_{-2}$ , most of the surface mass density of an NFW (or SIS) halo is determined by masses whose mass density has a slope of  $\sim -2$ , the contribution of masses at inner regions whose mass density has a slope of  $\sim -1$  is small. Then the surface mass density can be approximately written as

$$\Sigma_s(R_{2D}, m) \sim m^{-\alpha} R_{2D}^{\alpha\beta} R_{-2}^{-1}. \quad (12)$$

Assuming that  $\alpha \sim \beta \sim 1$  for NFW haloes, equation (12) gives  $\Sigma_s(R_{2D}, m) \approx m^{-\alpha}$ . Thus  $\Sigma_s$  does not depend on  $R_{2D}$ . Setting  $R_{2D} = 0$ , we can obtain an approximated formula for the surface mass density at  $R_{2D} \lesssim R_E$ ,

$$\begin{aligned}
 \Sigma_s(R_E) &\approx \frac{\mu_*^\alpha m_0^{\alpha-1}}{1-\alpha} \left[ m_{max}^{1-\alpha} - m_{min}^{1-\alpha} \right] \\
 &\times e^{\sigma^2 \alpha^2 / 2} J[\gamma, R_{200}, C; z], \quad (13)
 \end{aligned}$$

and

$$\begin{aligned}
 n_s(R_E) &\approx \frac{\mu_*^\alpha m_0^{\alpha-1}}{\alpha} \left[ -m_{max}^{-\alpha} + m_{min}^{-\alpha} \right] \\
 &\times e^{\sigma^2 \alpha^2 / 2} J[\gamma, R_{200}, C; z], \quad (14)
 \end{aligned}$$

where

$$\begin{aligned}
 J[\gamma, R_{200}, C, z] &\equiv 2\pi A_{acc} B f_s (1-\gamma) \csc(\gamma\pi) R_{200} \\
 &\times C^{-(1+\gamma)} \delta_c(C) \rho_{crit}(z). \quad (15)
 \end{aligned}$$

Here a condition  $0 < \gamma < 2$  should be satisfied in order to avoid divergence.

The surface mass density of an NFW lensing galaxy halo is given by

$$\begin{aligned}
 \Sigma_0(R_{2D}) &= \left[ \frac{2R_{-2}^3}{R_{2D}^2 - R_{-2}^2} + \frac{4R_{-2}^4}{(R_{-2}^2 - R_{2D}^2)^{3/2}} \right. \\
 &\times \left. \operatorname{arccoth} \left[ \frac{R_{2D} + R_{-2}}{(R_{-2}^2 - R_{2D}^2)^{1/2}} \right] \right] \delta_c(C) \rho_{crit}(z). \quad (16)
 \end{aligned}$$

Then, the ratio of the convergence of subhaloes  $\kappa_s$  to that of the host NFW halo  $\kappa_0$  can be obtained from equations (3)-(11) and (16). As shown in Fig. 2, the ratio increases in  $R_{2D}$ . At  $R_{2D}/R_{200} \sim 0.01$ , the dependence on  $R_{2D}$  is determined solely by the surface mass density of an NFW host halo as  $\kappa_s$  is nearly constant. The slope is slightly flatter than  $R_{2D}^{-1}$ , because the effective Einstein radius is smaller than the scale radius  $R_{2D}/R_{200} \sim 0.01 < R_{-2}/R_{200} \sim 0.1$ . As we shall show later, the ratio  $\kappa_s/\kappa_0$  gives an upper limit for the dark matter fraction  $f$  at the position of lensed images, which characterizes the strength of contribution from subhaloes.

### 3 LINE-OF-SIGHT LENSING

To take into account the non-linear effects of line-of-sight structures, we first calculate the non-linear power spectra of matter fluctuations down to mass scales of  $\sim 10^5 h^{-1} M_\odot$  using  $N$ -body simulations (Inoue & Takahashi 2012; Takahashi & Inoue 2014). For simplicity, we do not consider baryonic effects in our simulations. In the following, we assume that the astrometric shifts of lensed images caused by perturbers are sufficiently smaller than the deflection angle of a background lens model and the strong lensing effects caused by perturbers are negligible. Then the magnification contrast  $\delta^{\bar{\mu}} = \delta\bar{\mu}/\bar{\mu}$  for each lensed image with a nonperturbed convergence  $\kappa$  and a shear  $\gamma$  can be approximated as

$$\delta^{\bar{\mu}} \approx \frac{2(1-\kappa)\delta\kappa + 2\gamma\delta\gamma}{(1-\kappa)^2 - \gamma^2}, \quad (17)$$

where  $\delta\kappa$  and  $\delta\gamma$  are the convergence and shear due to perturbers in the line of sight (Inoue & Takahashi 2012; Takahashi & Inoue 2014). Using equation (17), we can estimate the magnification contrast for each lens using semi-analytic formulae developed in Inoue & Takahashi (2012); Takahashi & Inoue (2014). We also take into account astrometric shifts due to line-of-sight structures, which are often overlooked in the literature. For details, see also Inoue et al. (2015).

### 4 QUADRUPLE LENS SYSTEMS

In this paper, we use 10 QSO-galaxy quadruple lens systems, namely, B1422+231, B0128+437, MG0414+0534, B1608+656, B0712+472, B2045+265, H1413+117, PG1115+080, Q2237+0305, RXJ1131-1231 and the SMG-galaxy system SDP.81. We exclude the spiral lens B1933+503, because it has a very complex structure. Similarly, we also exclude B1555+375 that has a disc component (Hsueh et al. 2016). However, we include Q2237+0305 as the bulge component of the spiral lensing galaxy seems

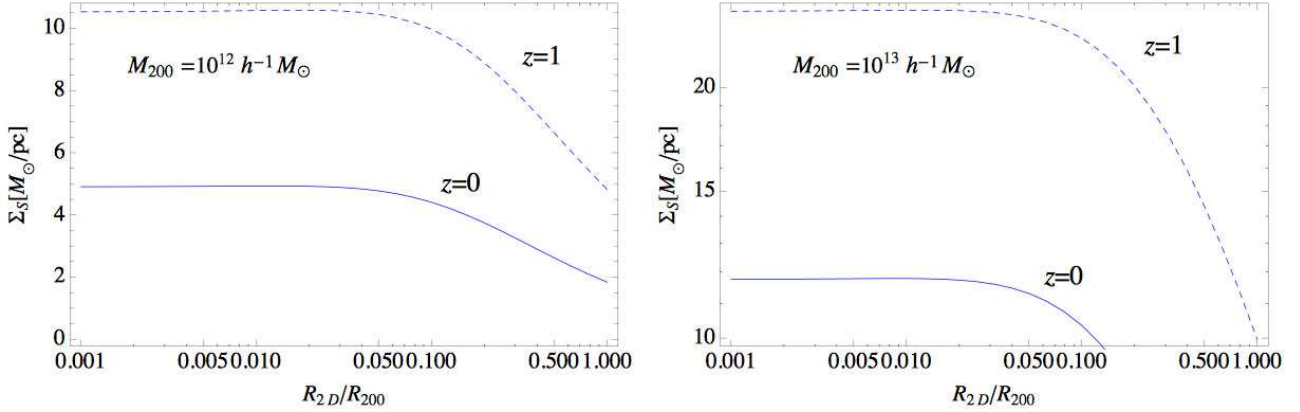


**Figure 1.** Surface mass density of subhaloes at a normalised distance  $R_{2D}/R_{200}$  for  $M_{200} = 10^{12} h^{-1} M_{\odot}$  (left) and  $M_{200} = 10^{13} h^{-1} M_{\odot}$  (right).

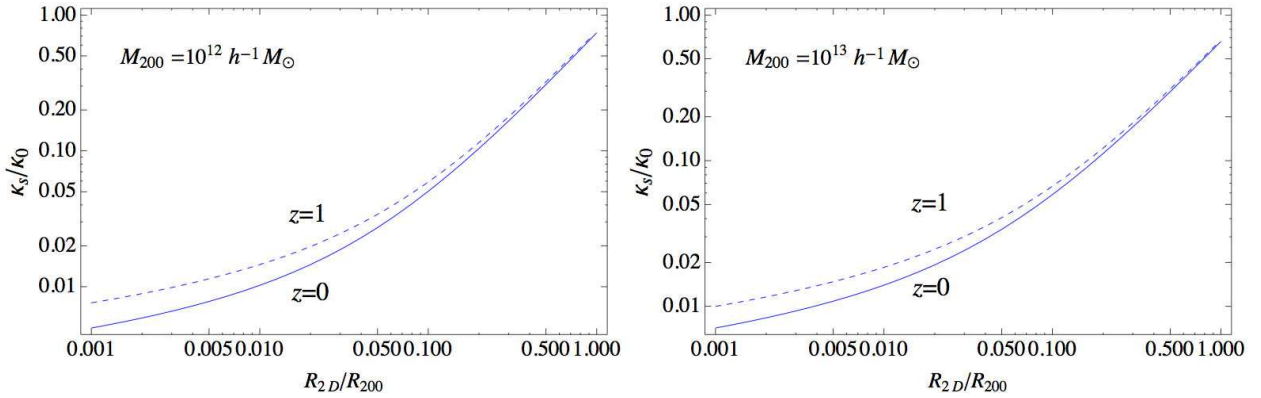


**Figure 2.** Ratio of the convergence of subhaloes to that of the host NFW halo at a normalised distance  $R_{2D}/R_{200}$  for  $M_{200} = 10^{12} h^{-1} M_{\odot}$  (left) and  $M_{200} = 10^{13} h^{-1} M_{\odot}$  (right).

to dominate over the disk component. In our analysis, we use observed MIR fluxes for MG0414+0534, H1413+117, PG1115+080, Q2237+0305 and RXJ1131-1231 and radio fluxes averaged over a certain period for B1422+231, B0128+437, B1608+656, B0712+472, and B2045+265. For the astrometry of lensed images and the centroids of lensing galaxies, we use optical or NIR data except for SDP.81 in order to avoid bias due to complex structures of jets. We also use time delay for modeling B1608+656<sup>2</sup>. For SDP.81, we use the processed archival image of the band 7 continuum taken from the ALMA Science Portal (see [ALMA Partnership et al. \(2015\)](#) for detail) and for the flux ratios of lensed images, we use fluxes in an aperture radius 0.04 arcsec defined in the source plane. For detail of these 11 lens systems, see [Takahashi & Inoue \(2014\)](#); [Inoue et al. \(2015, 2016\)](#).

In table 1, we show the redshifts of the source  $z_S$  and those of the primary lens  $z_L$ , the observed wavelength band of position and flux of lensed images, the number of lensed images  $N$  used for constraining the lens model. The radius

$R_S$  of a MIR continuum source is estimated using dust reverberation, and  $R_S$  of a radio source is estimated from the apparent angular size (typically  $1 \sim 3$  mas in radius) of the lensed very long baseline interferometry images. For SDP.81, we adopt the beam size in the ALMA band 7 continuum image as the source size, though it may have a smaller structure. The wavenumber is defined as  $k_S \equiv 2\pi/(4r_S)$ , where  $r_S$  is the comoving radius of a source.  $k_S$  is used as the upper limit of wavenumber in estimating  $\eta$  from line-of-sight structures.

## 5 LENS MODEL

As a fiducial model of a primary lensing galaxy halo, we adopt a singular isothermal ellipsoid (SIE) ([Kormann et al. 1994](#)), which can explain flat rotation curves. There is considerable evidence in favor of the isothermal profile, and the properties of gravitational potential near the Einstein radius are insensitive to the radial mass distribution ([Koopmans et al. 2009](#); [Humphrey & Buote 2010](#); [Barnabè et al. 2011](#); [Oguri et al. 2014](#)). We use the fluxes of lensed images, the relative positions of lensed quadruple images and the centroid of lensing galaxies, and the time delay of lensed images if available. The contribution from

<sup>2</sup> We did not take into account the effect of substructures for estimating the time delay in our analysis ([Keeton & Moustakas 2009](#)), since the observational errors ( $\sim 5\%$ ) are too large to distinguish the perturbative effect.

groups, clusters, and large-scale structures at angular scales larger than the Einstein angular radius of the primary lens is taken into account as an external shear (ES). The parameters of the SIE('s) plus ES model are the effective Einstein radius  $b$  (defined in Kormann et al. (1994)), the apparent ellipticity  $e$  of the lens and its position angle  $\theta_e$ , the strength and the direction of the external shear ( $\gamma, \theta_\gamma$ ), the lens position  $(x_G, y_G)$ , and the source position  $(x_s, y_s)$ . The Hubble constant  $h$  is also treated as a model parameter. The angles  $\theta_e$  and  $\theta_\gamma$  are measured in East of North expressed in the observer's coordinates. We modeled secondary lenses in MG0414+0534, H1413+117, B1608+656 and B2045+265 by either an SIS or SIE.

To find a set of best-fit parameters, we use a numerical code GRAVLENS<sup>3</sup> developed by Keeton in order to implement the simultaneous  $\chi^2$  fitting of the fluxes, positions, and time delay of lensed images (if reliable data is available) and the positions of centroid of lensing galaxies. The best-fitted model parameters are in Inoue & Takahashi (2012); Takahashi & Inoue (2014).

## 6 METHOD

In order to measure the magnification perturbation of lensed images, we use a statistic  $\eta$  defined as

$$\eta \equiv \left[ \frac{1}{2N_{\text{pair}}} \sum_{i \neq j} \left[ \delta_i^{\tilde{\mu}}(\text{minimum}) - \delta_j^{\tilde{\mu}}(\text{saddle}) \right]^2 \right]^{1/2}, \quad (18)$$

where  $\delta_i^{\tilde{\mu}}(\text{minimum})$  and  $\delta_j^{\tilde{\mu}}(\text{saddle})$  are magnification contrasts corresponding to the minimum and saddle images and  $N_{\text{pair}}$  denotes the number of pairs of lensed images. If the correlation of magnification between pairs of images is negligible, then  $\eta$  corresponds to the mean magnification perturbation per a lensed image. Perturbation by locally over-dense structures would boost  $\eta$  as the saddle images tend to be demagnified whereas the minimum images are always magnified provided that the strong lensing effect is negligible. Note that we need to fix the primary lens model (i.e., a best-fitted model without line-of-sight structures or subhaloes) in order to calculate  $\eta$ . In other words,  $\eta$  is a model dependent statistic though it can be calculated from the observed flux ratios.

The mean and the standard deviation of  $\eta$  can be calculated as follows. First, we estimate the perturbation  $\varepsilon$  of the largest angular separation  $\theta_{\text{max}}$  between a pair of lensed images X and Y,

$$\varepsilon = |\delta\theta(X) - \delta\theta(Y)|, \quad (19)$$

where  $\delta\theta$  represents the astrometric shift of a lensed image at  $\theta$  in the lens plane. We then assume that the perturbation satisfies  $\varepsilon \leq \varepsilon_0$  where  $\varepsilon_0$  is the observational error for the largest angular separation. This condition gives an approximated upper limit on the contribution of line-of-sight structures or subhaloes assuming that the gravitational potential of the primary lens is similar to that of an SIS and sufficiently smooth on the scale of the effective Einstein radius (see appendix). Note, however, that if an astrometric shift caused by a possible local perturber is parallel to the

tangential arc of a lensed image, though the possibility is small for a point source, the condition is too strict to some extent<sup>4</sup>.

In the case of lensing by line-of-sight structures, we also assume that small-scale modes with a wavelength larger than the mean comoving separation  $\langle b \rangle$  between the lens center and lensed images in the primary lens plane are significantly suppressed. The reason is that any modes whose fluctuation scales are larger than  $\langle b \rangle$ , which is roughly the size of the comoving effective Einstein radius, contribute to the smooth components of a primary lens, namely, constant convergence and shear. Therefore, we consider only modes whose wavenumbers satisfy  $k > k_{\text{lens}}$  where  $k_{\text{lens}} \equiv \pi/(2\langle b \rangle)$ . Even if the cutoff is applied, sometimes the condition  $\varepsilon \leq \varepsilon_0$  cannot be satisfied due to a presence of a possible secondary lens or other lenses. In this case, we further cutoff the small-scale fluctuations with a wavenumber  $k > k_{\text{lens}}$  using the so-called ‘‘constant-shift (CS) cut’’ (Takahashi & Inoue 2014). Roughly speaking, the CS cut leads to a uniform suppression of astrometric shift from fluctuations with wavenumbers of  $k_{\text{lens}} < k < k_{\text{cut}}$ . Using the non-linear power spectrum with the CS cut, we can estimate the second moment of  $\langle \eta^2 \rangle$ . From the fitted function of  $\eta$  in (Takahashi & Inoue 2014), we can obtain a simple formula  $\langle \eta \rangle \sim 0.85 \langle \eta^2 \rangle^{1/2}$  and the standard deviation  $\delta\eta = 0.53 \langle \eta^2 \rangle^{1/2}$ , which agrees with the fitted function within a percent level for  $\langle \eta^2 \rangle^{1/2} < 0.2$ . Note that the particle masses in our  $N$ -body simulations are  $\sim 10^5 h^{-1} M_\odot$ , which can resolve mass fluctuations at the comoving scale of  $\sim 1$  kpc.

In the case of substructure lensing, we assume that subhaloes at the time of infall have an NFW profile. Moreover, we also assume that subhaloes that yield astrometric shifts (at  $r \sim r_{-2}$ ) larger than  $\varepsilon_0$  at the time of infall do not perturb the lens system. From this constraint, we can determine the maximum mass of a perturbing subhalo  $m_{200}^{\text{max}}$ . These assumptions are reasonable ones as long as the relevant subhaloes in the neighbourhood of lensed images have a mass profile similar to an SIS. In fact, the effect of outer profiles  $r > r_{-2}$  of an NFW subhalo can be neglected. The reason is as follows. As we shall show in the next section (Correa et al. 2015), the typical mass scale of subhaloes that can maximally perturb the positions of lensed images is  $\sim 10^9 M_\odot$ . At the typical infall redshift  $z_{\text{infall}} \sim 2$ , the concentration parameter is  $C \sim 7$ , which corresponds to  $r_{-2} \sim 3$  kpc. Thus, the size of the region in which the relevant NFW subhaloes have a density profile with a slope of  $-2$  is comparable to  $\langle b \rangle \sim 5$  kpc in our quadruple lens samples. This suggests that these NFW haloes are kept far from the primary (and the secondary) lens and their effects are limited to changing modes whose wavelengths are larger than  $\langle b \rangle$ . Moreover, for  $r > r_{-2}$ , the astrometric shifts are smaller than those at  $r \sim r_{-2}$ . Note, however, that we also assume that the density profile of these massive subhaloes at  $r \sim r_{-2}$  does not change so much after infall. Although the tidal heating causes a concentration of subhalo mass near the center, most of light rays pass through the outer region of subhaloes

<sup>4</sup> Some systems with an extended source show an Einstein ring in which the magnification is significantly large. In this case, perturbers in the line of sight to the ring (if present) can cause degeneracy with the macromodel.

<sup>3</sup> See <http://redfive.rutgers.edu/~keeton/gravlens/>

where the effect of tidal heating is much small. Therefore, we expect that the change of inner mass profile is also not relevant to the astrometric perturbation.

We also neglect masses below  $m_{200}^{\min}$  for which the perturbation to the magnification caused by a corresponding SIS (having the same astrometric shift at  $r = r_{-2}$ ) centred at a source is less than  $\sim 0.1$  percent due to the finite source size  $R_S$ . In our analysis, for the unperturbed lens component, we use  $M_{200}$  to make correspondence between a best-fitted SIE profile and an NFW profile.

In order to estimate the mass profile of subhaloes at the time of infall, we use a semi-analytic model of NFW haloes (only dynamically relaxed ones) in which the concentration parameter  $C = C(m_{200}, z_{\text{infall}})$  is given by

$$\begin{aligned} \log_{10} C &= a + b \log_{10}(m_{200}/M_{\odot}) [1 + c(\log_{10}(m_{200}/M_{\odot}))^2], \\ a &= 1.7543 - 0.2766(1+z) + 0.02039(1+z)^2, \\ b &= 0.2753 + 0.00351(1+z) - 0.3038(1+z)^{0.0269}, \\ c &= -0.01537 + 0.02102(1+z)^{-0.1475}, \end{aligned} \quad (20)$$

where  $z_{\text{infall}} \leq 4$  (Correa et al. 2015). Note that this relation is also used for calculating  $M_{200}$  and  $R_{200}$  for the lensing galaxy haloes.

As for the infall redshift, we assume that  $0 < z_{\text{infall}} < 4$  and the mean is given by  $\langle z_{\text{infall}} \rangle \sim 2$  (Emberson et al. 2015). Since the infall redshift  $z_{\text{infall}}$  of massive subhaloes tends to be smaller than this value, we take the ambiguity of  $\Delta z_{\text{infall}} = 2$  into account in estimating the mean of the convergence perturbation  $\delta\kappa$  due to subhaloes.

For estimating the shear perturbation  $\delta\gamma$ , we assume statistical isotropy for the perturbation. Then we have  $|\delta\gamma| \sim |\delta\kappa|$  and we can estimate the magnification contrast  $\delta\mu$  and  $\langle \eta \rangle$  for subhaloes. In a similar manner, assuming statistical isotropy, we can estimate the strength of the convergence perturbation  $|\delta\kappa|$  from the observed  $\eta$ . Note that the relation is exact for SISs. Furthermore, we neglect a possible spatial correlation between perturbers at different positions of lensed images. The explicit form of calculation is written as follows. Let us consider a lens with bright images A (minimum), B (saddle), and C (minimum). In terms of observed fluxes  $\mu_A, \mu_B, \mu_C$  and unperturbed fluxes  $\mu_{A0}, \mu_{B0}, \mu_{C0}$  from a best-fitted model, the estimator of  $\eta$  is given by

$$\hat{\eta}^2 = \frac{1}{4} \left[ \left( \frac{\mu_A \mu_{B0}}{\mu_{A0} \mu_B} - 1 \right)^2 + \left( \frac{\mu_C \mu_{B0}}{\mu_{C0} \mu_B} - 1 \right)^2 \right]. \quad (21)$$

Assuming statistical isotropy, we have

$$\hat{\eta}^2 \sim \frac{1}{4} (I_A + 2I_B + I_C) \delta\kappa^2, \quad (22)$$

where

$$I_i \equiv \mu_i^2 (4(1 - \kappa_i)^2 + 2\gamma_i^2), \quad \text{for } i = A, B, C, \quad (23)$$

and  $\kappa_i, \gamma_i$  are the non-perturbed convergence and the shear at the position of a lensed  $i$ -image. Thus, we can estimate  $|\delta\kappa|$  from lensed images and a best-fitted model.

In the case of line-of-sight structures, we find that the correlation effect is  $\sim 10$  percent for lenses with a fold caustic and much smaller for those with a cusp caustic. Thus, this approximation yields at most  $\sim 10$  percent errors in  $|\delta\kappa|$  estimated from  $\eta$ . In the case of subhaloes, we expect that the spatial correlation on scales of  $< 10$  kpc is negligible after infalling to the center of a host halo because of the strong tidal force acting on them.

## 7 RESULT

Firstly, we show the magnification perturbation per a lensed image  $\eta$  in figure 3. The expected contribution  $\eta \sim 0.05$  from subhaloes is not sufficient to explain the observed values  $\eta \sim 0.10$  especially for lens systems with a high source redshift  $z_S > 3$ . Although the expected contribution  $\eta \sim 0.1$  from line-of-sight structures is sufficient for explaining observed values, the addition of contribution from subhaloes improves the fit especially for systems with a low redshift  $z_L < 1.5$  and the overall fit still remains good.

Secondly, we show the strength of convergence perturbation  $|\delta\kappa|$  in  $z_S$  assuming statistical isotropy for perturbations in figure 4. The observed values (red disks) seem to increase with the source redshift  $z_S$ . This is consistent with an interpretation that the dominant contribution comes from the line-of-sight structures (blue diamonds), because the surface density increases with the comoving length to the source. On the other hand, the correlation between  $\delta\kappa$  from subhaloes and  $z_S$  seems to be weak (blue disks). Out of 11 samples, MG0414+0534 shows the largest convergence perturbation  $\delta\kappa = 0.0059_{-0.0004}^{+0.0006}$  from subhaloes. Note that the ambiguity in the infall redshift of subhaloes induces errors of just 5 to 10 percent in  $\langle |\delta\kappa| \rangle$ , which fall within the size of circles in figure 4. However, the observed value  $|\delta\kappa_{\text{obs}}| = 0.011 \pm 0.003$  is much larger. For other systems, the convergence perturbation due to subhaloes is much smaller and more difficult to fit to the data. The mean value for the subhaloes is  $\langle \delta\kappa_{\text{sub}} \rangle = 0.003$  whereas that for the line-of-sight structures is  $\langle |\delta\kappa_{\text{los}}| \rangle = 0.008$  and that for the observed values is  $\langle |\delta\kappa_{\text{obs}}| \rangle = 0.009$ . Using the mean convergence at the positions of lensed images in the best-fitted model, the mean of the ratio of a projected dark matter mass fraction in subhaloes is just  $\langle f_{\text{sub}} \rangle = 0.006$  whereas that for the line-of-sight structures is  $\langle f_{\text{los}} \rangle = 0.017$  and that for the observed values is  $\langle f_{\text{obs}} \rangle = 0.019$ . Thus, it is difficult to explain the observed convergence perturbations by contribution from only subhaloes.

Thirdly, we show the strength of convergence perturbation  $|\delta\kappa|$  in  $z_L$  assuming statistical isotropy for perturbations in figure 5. It seems that it is consistent with an interpretation that the dominant contribution comes from subhaloes. This may be due to the fact that  $R_E/R_{200}$  increases with  $z_L$  (figure 6). The reason is as follows. Suppose that the effective Einstein angular radius  $\theta_E \sim 1''$  is constant. Then, the effective Einstein radius  $R_E = D_L \theta_E$  increases in  $z_L$  until  $z_L \sim 1.5$  (blue curve in figure 6). Then  $R_E$  begins to decrease slowly due to cosmic expansion. For  $z_L < 2.0$ , however, this effect is small. As we have shown in section 2, the ratio of convergence perturbation of subhaloes  $\delta\kappa = \kappa_S$  to the convergence  $\kappa_0$  of the lensing galaxy halo increases with  $R_E = R_{2D}$ . Since  $\kappa_0 \sim 0.5$  (i.e., the lensed images are near the critical curve in an SIE), we expect that  $\delta\kappa$  increases with  $R_E$  hence,  $z_L$  until  $z_L \sim 1.5$ . However, the expected strength is just  $|\delta\kappa| \lesssim 0.005$  whereas the observed values are  $|\delta\kappa| \lesssim 0.001$ . As shown in the upper right panel in figure 5, the contribution from line-of-sight structures have a weak dependence on  $z_L$ . This dependence may come from a weak correlation between  $z_S$  and  $z_L$ . For a given  $z_S$ , the possibility of a strong lensing is maximum at  $z_L$  where the critical surface density  $\Sigma_{\text{crit}}$ , which is inversely proportional to  $L = D_L D_S / D_{LS}$ , is the lowest. In figure 7, we plotted

**Table 1.** Quadruple Lens Systems

lens system	$z_S$	$z_L$	position	flux	$N$	$b''$	$\langle \kappa \rangle$	$\log_{10} k_S (h/\text{Mpc})$	$R_E (\text{kpc})$	$R_{200} (\text{kpc})$	$M_{200}$	$m_{200}^{\max}$	$m_{200}^{\min}$	reference
B1422+231	3.62	0.34	opt/NIR	radio	3	0.78	0.40	4.8	3.9	320	$3.4 \times 10^{12}$	$1.1 \times 10^8$	$6.6 \times 10^3$	(1) (2)
B0128+437	3.124	1.145	opt/NIR	radio	4	0.24	0.52	4.0	2.1	150	$9.2 \times 10^{11}$	$1.3 \times 10^9$	$7.1 \times 10^4$	(1) (3) (4)
SDP.81	3.042	0.2999	submm	submm	4	1.6	0.50	3.7	7.4	470	$1.0 \times 10^{13}$	$2.8 \times 10^7$	$4.3 \times 10^5$	(13)
MG0414+0534	2.639	0.96	opt/NIR	MIR	4	1.1	0.55	4.9	9.0	350	$9.0 \times 10^{12}$	$1.2 \times 10^9$	$3.3 \times 10^3$	(5) (6) (7)
H1413+117	2.55	1.88(★)	opt/NIR	MIR	4	0.57	0.54	5.5	4.9	270	$1.1 \times 10^{13}$	$6.2 \times 10^9$	$1.0 \times 10^3$	(5) (10)
PG1115+080	1.72	0.31	opt/NIR	MIR	2	1.1	0.52	6.0	5.4	410	$7.0 \times 10^{12}$	$6.0 \times 10^8$	$1.6 \times 10^2$	(5) (11)
Q2237+0305	1.695	0.04	opt/NIR	MIR	4	0.9	0.54	7.1	0.74	370	$3.8 \times 10^{12}$	$4.1 \times 10^8$	$3.4 \times 10^1$	(5) (6)
B1608+656	1.394	0.63	opt/NIR	radio	4	0.91	0.67	3.5	6.4	390	$8.6 \times 10^{12}$	$5.6 \times 10^8$	$5.8 \times 10^3$	(2) (8)
B0712+472	1.339	0.406	opt/NIR	radio	3	0.77	0.50	4.8	4.3	350	$4.8 \times 10^{12}$	$1.5 \times 10^9$	$7.8 \times 10^3$	(1) (5)
B2045+265	1.28	0.8673	opt/NIR	radio	4	0.791	0.39	4.9	8.4	490	$2.3 \times 10^{13}$	$6.1 \times 10^8$	$9.8 \times 10^3$	(1) (9)
RXJ1131-1231	0.658	0.295	opt/NIR	MIR(★★)	3	1.8	0.44	3.9	8.4	640	$2.5 \times 10^{13}$	$1.0 \times 10^9$	$4.9 \times 10^5$	(5) (12)

Note: The unit of mass for  $M_{200}$ ,  $m_{200}^{\max}$  and  $m_{200}^{\min}$  is  $h^{-1}M_{\odot}$ . (★): The lens redshift  $z_L$  is obtained from a best-fit model. (★★): The flux of a line emission [OIII]. References: (1) Koopmans et al. (2003) (2) Sluse et al. (2012) (3) Biggs et al. (2004) (4) Lagattuta et al. (2010) (5) CASTLES data base: <http://www.cfa.harvard.edu/castles> (6) Minezaki et al. (2009) (7) MacLeod et al. (2013) (8) Fassnacht et al. (2002) (9) McKean et al. (2007) (10) MacLeod et al. (2009) (11) Chiba et al. (2005) (12) Sugai et al. (2007) (13) (Inoue et al. 2016)

**Table 2.** Linear Model Fit of Subsamples (corresponding to red dotted and red dashed lines in right panels in figure 8)

subsample	$\alpha$	$p$ - value	$\beta$	$p$ - value
$z_S > 2$ (with error)	$0.0075 \pm 0.0020$	0.031	$0.0046 \pm 0.0052$	0.45
$z_S > 2$ (without error)	$0.0065 \pm 0.0025$	0.078	$0.0046 \pm 0.0023$	0.13
$z_L > 0.6$ (with error)	$-0.0007 \pm 0.0017$	0.72	$0.0046 \pm 0.0009$	0.014
$z_L > 0.6$ (without error)	$-0.0002 \pm 0.0023$	0.95	$0.0048 \pm 0.0010$	0.018

redshifts  $z_S$ ,  $z_L$  of 11 samples with contours of  $L$ , which can be regarded as the PDF of strong lensing. Although the sample is sparse, the histogram of angles  $\theta = z_L/z_S$  has its peak at  $\theta = 10 - 20^\circ$ , which is consistent with the result obtained from  $L$  integrated along  $\theta$ . Thus, it is reasonable to conclude that the weak  $z_L$  dependence of  $\delta\kappa$  comes from line-of-sight structures as well as subhaloes.

Finally, we show an imprint of difference in the redshift dependence of  $|\delta\kappa|$  between  $z_S$  and  $z_L$ . In order to determine the origin of anomaly in the flux ratios, we separate the data into a low  $z_L < 0.6$  and a high  $z_L > 0.6$  subsamples and a low  $z_S < 2$  and a high  $z_S > 2$  subsamples. As one can see in figure 8, a high  $z_L > 0.6$  sample shows a strong correlation between  $z_S$  and the observed  $\delta\kappa$  whereas a high  $z_S > 2$  sample shows a weak correlation between  $z_L$  and the observed  $\delta\kappa$ . The other subsamples do not show any sign of correlation. In order to measure the correlation between the redshift and the convergence perturbation, we fit the data with a linear function  $|\delta\kappa| = \alpha + \beta z_L(z_S)$ , where  $\alpha$  is the base function and  $\beta$  is the gradient. As shown in table 2, for subsamples with  $z_L > 0.6$ , a null hypothesis that  $\beta = 0$  (no correlation) can be rejected at a 98 ~ 99 percent confidence level. On the other hand, for subsamples with  $z_S > 2$ , the null hypothesis

( $\beta = 0$ ) cannot be rejected at a 90 percent confidence level. The difference shows that the contribution from line-of-sight structures is indeed much larger than that from subhaloes. The apparent correlation between the observed  $|\delta\kappa|$  and  $z_L$  is not statistically significant.

## 8 ANOMALOUS ANOMALY

If line-of-sight structures are the primary cause of the flux ratio anomaly, we expect a contribution from positive and negative density perturbations almost equally after subtracting the convergence averaged within the effective Einstein radius (Takahashi & Inoue 2014). This is due to the spatial correlation in density fluctuations on scales  $\lesssim 1\text{kpc}$ . In the CDM models, the cosmic web structures appear on all the scales that exceed the free-streaming scale. Therefore, any clumps formed on walls and filaments should have spatial correlations between them. Moreover, intergalactic medium may reside along these structures and enhance the lensing effect by these clumps due to radiative cooling. On the other hand, most subhaloes at an effective Einstein radius  $R_E$  are tidally disrupted. Then, the spatial correlation

between subhaloes are expected to be suppressed, leading to a reduction in the contribution from negative density perturbations. Thus, if the contribution from subhaloes is large, we expect that lensed images of minimum in the arrival time surface tend to be magnified. However, if the contribution from line-of-sight structures is large, *there is a  $\sim 50$  percent chance of demagnification in minimum images*. If this is the case, the probability of observing such an “anomalous anomaly” increases with the source redshift  $z_S$ . In order to estimate the probability, we calculate the ratio of the mean strength of convergence perturbation  $\delta\kappa$  from subhaloes to that from the total (subhaloes and line-of-sight structures). The contribution from subhaloes is  $\sim 40$  percent of the total at a source redshift  $z_S = 0.7$  and decreases monotonically in  $z_S$  to  $\sim 20$  percent at  $z_S = 3.6$  (figure 9). Assuming that demagnification of a minimum is always caused by line-of-sight structures with a 50 percent of chance, the probability is  $\sim 30$  percent for  $z_S = 0.7$  and  $\sim 50$  percent for  $z_S = 3.6$ , the possibility of finding such an “anomalous anomaly” is expected to be  $\sim 30$  percent for  $z_S = 0.7$ , and  $\sim 40$  percent for  $z_S = 3.6$ . Out of 11 samples, systems with a flux ratio anomaly at more than  $3\sigma$  level are B1442+231, MG0414+0534, and SDP.81. The “anomalous anomaly” is found in B image of SDP.81 (Inoue et al. 2016). Therefore, the probability is  $\sim 30$  percent and hence consistent with the prediction. Although the number of current sample is too small to verify this interpretation, a significant increase in the number of quadruple lenses will lead to discoveries of such a new type of anomaly in the near future.

## 9 CONCLUSION AND DISCUSSION

In this paper, we have explored the origin of the observed flux ratio anomaly in quadruple lensing systems. Firstly, based on a semi-analytical formula, we have shown that the surface mass density of subhaloes are nearly constant at the inner region  $R_{2D} < R_{-2}$  of a host galaxy halo where the light-ray of lensed images pass through. Then we found that the expected contribution from subhaloes is not sufficient to explain the observed anomalies especially for lens systems with a high source redshift  $z_S > 3$ . Although the expected contribution from line-of-sight structures is already sufficient for explaining observed flux ratios, the addition of contribution from subhaloes improves the fit especially for systems with a low redshift  $z_L < 1.5$ . Secondly, assuming statistical isotropy in perturbations, the measured convergence perturbation seems to increase with the source redshift  $z_S$  as well as the lens redshift  $z_L$ . Thirdly, we have shown that the observed correlation between measured convergence perturbations with  $z_S$  is statistically significant at a 98-99 percent confidence level whereas that with  $z_L$  is not statistically significant at a 90 percent confidence level. This result supports an idea that the dominant contribution comes from line-of-sight structures rather than subhaloes. We have discussed a possible origin of correlations based on a semi-analytic formula. Finally, we have shown that if the contribution from line-of-sight structures is dominant, 30-40 percent of minimum images that show anomaly in the relative flux would be systematically demagnified. The number of systems showing such an “anomalous anomaly” first found in

SDP.81 (Inoue et al. 2015) would increase with the source redshift  $z_S$ .

Our result for substructure lensing is consistent with the previous result, which was obtained using  $R_{\text{cusp}}$  and  $R_{\text{fold}}$  (Xu et al. 2015). Out of 11 lenses, MG0414+0534 showed the largest convergence perturbation  $\delta\kappa = 0.0059$  from subhaloes but the value is too small to account for the observed flux ratios. We have taken into account the astrometric shifts due to subhaloes and use a weak+strong lens decomposition assuming a smooth potential that is similar to an SIS (or SIE) for modeling the unperturbed primary lens. Although our approach suffers from inadequate lens modeling, systematic errors due to the magnification bias and extra lenses do not affect our constraints. Our obtained value for the mean substructure mass fraction  $\langle f_{\text{sub}} \rangle = 0.006$  is consistent with the value  $f_{\text{sub}} = 0.0064^{+0.0080}_{-0.0042}$  obtained from SLAC lenses for a substructure mass function slope  $\alpha = 0.90$  ( $\tilde{\alpha} = 1.90$ ) (Vegetti et al. 2014). Thus, as long as baryonic physics does not significantly affect the result, it is reasonable to conclude that CDM substructures are not the entire reason for the flux anomaly problem.

On the other hand, our result for line-of-sight lensing significantly differs from the result which was obtained using  $R_{\text{cusp}}$  and  $R_{\text{fold}}$  (Xu et al. 2012). The difference may come from the typical source redshift  $z_S = 2$  assumed in Xu et al. (2012). In fact, our result indicates that for  $z_S < 2$ , the ratio of the strength of convergence perturbation from subhaloes to that of the total value is 30 to 40 percent. For higher source redshifts, however, the ratio becomes much smaller. Moreover, the two lens systems B2045+265 and B1555+375 used in (Xu et al. 2012) (the latter was excluded in our analysis), which have a relatively large  $R_{\text{cusp}} = 0.4 \sim 0.5$  show another source of anomaly: B2045+265 has a secondary lens (McKean et al. 2007) and B1555+375 has an edge-on disk component that can account for the anomaly (Hsueh et al. 2016). Excluding these complex lenses would surely weaken the discrepancy with our result. Complex lens environments such as secondary lenses and disk components and neighbouring groups and clusters should be taken into account properly.

Our result indicates that a secondary lens can reside in the intergalactic space and not necessarily a companion of the primary lens. Furthermore, the previously claimed subhalo with a mass of  $(1.9 \pm 0.1) \times 10^8 M_\odot$  discovered from the residual image of an Einstein ring in B1938+666 (Koopmans 2005; Vegetti et al. 2012) may not be the subhalo of the primary lensing galaxy halo. It can be isolated from any haloes or belonging to another distant one. In order to measure the redshift of a secondary or that of a third lens, we can use the distortion pattern of an extended source and future submillimetre observations would be able to detect such small signals (Inoue & Chiba 2005b,a). With the aid of Atacama Large Millimetre/Submillimetre Array (ALMA), detection of other “anomalous anomaly” in lensed quadruple SMGs will be achieved by increasing the number of anomalous targets to  $\gtrsim 10$ , which can test our findings.

In our analysis, we assumed that primary lenses are described by SIEs as indicated by the surface brightness of the lensing galaxies. This assumption may be too simple. We did not take into account slight smooth distortion of the lens potential, such as low-order multipoles  $m_3$  and  $m_4$  or deviation from isothermal profile. As long as these complex

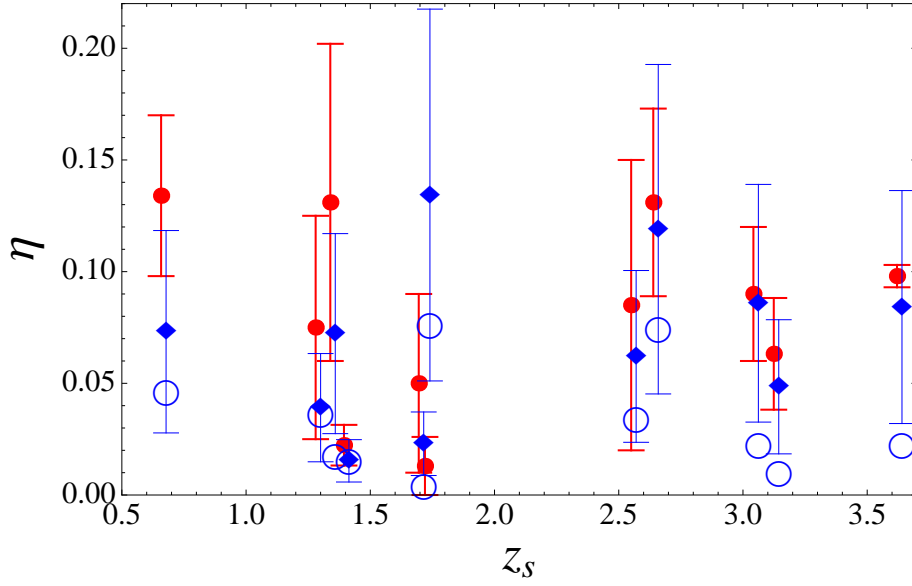


**Figure 3.** Magnification perturbation  $\eta$  versus the source redshift  $z_s$  for 11 quadruple lens samples. Red disks are observed values estimated from the best-fitted models with one-sigma observational error bars. Blue diamonds show the expected contribution from line-of-sight structures with one-sigma error bars. Blue circles show the expected contribution from subhaloes in lensing galaxy haloes. The positions of  $z_s$  for the expected values (blue) are slightly shifted for an illustrative purpose.

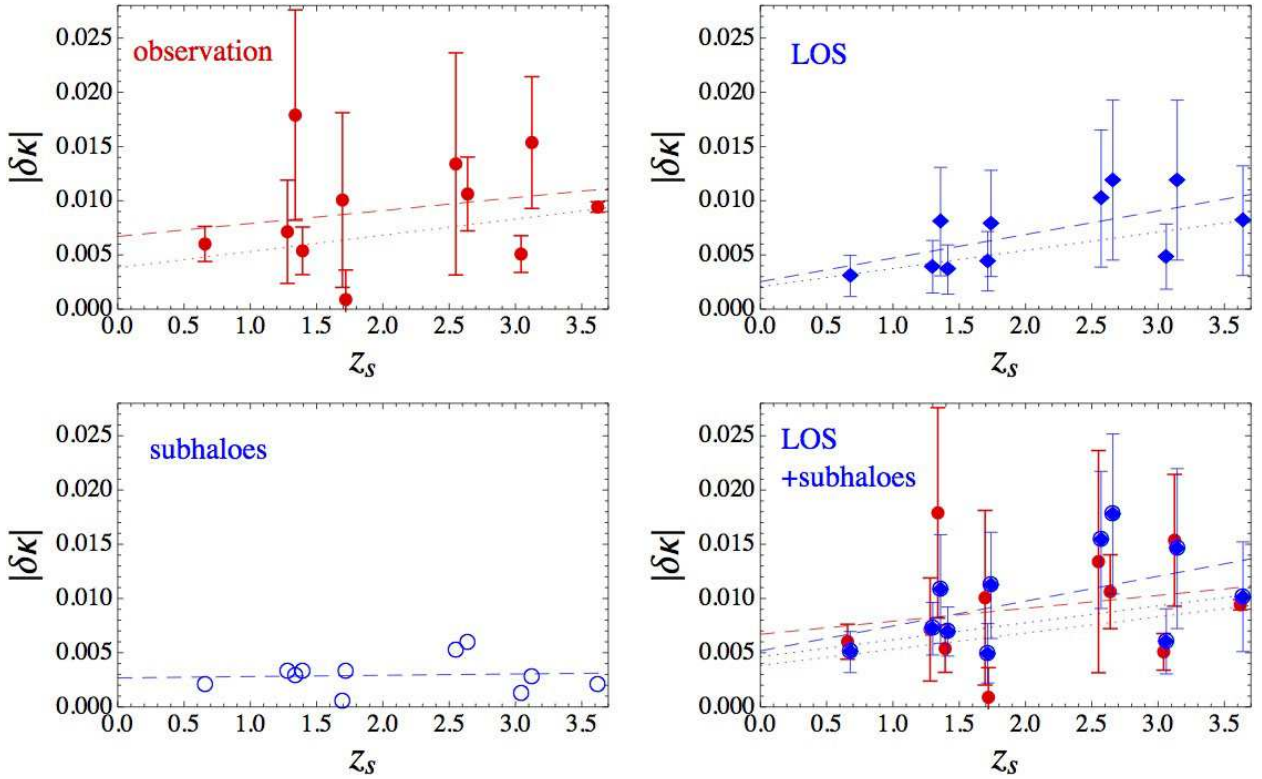


**Figure 4.** The strength of convergence perturbation  $\delta\kappa$  versus the source redshift  $z_s$  for 11 quadruple lens samples. The red disks are observed values estimated from the best-fitted models with one-sigma observational error bars. The blue diamonds show the expected contribution from line-of-sight structures with one-sigma theoretical error bars. The blue circles show the expected contribution from subhaloes in a lensing galaxy halo. The errors due to the ambiguity in the infall time of subhaloes are smaller than the size of the blue circles. The blue diamonds embedded in a blue circle show the expected contribution from line-of-sight structures plus subhaloes with one-sigma error bars. Red dotted and red dashed lines correspond to linear model fits to the observed values with and without taking into account the observational errors, respectively. The positions of  $z_s$  for the expected values (blue) are slightly shifted for an illustrative purpose.

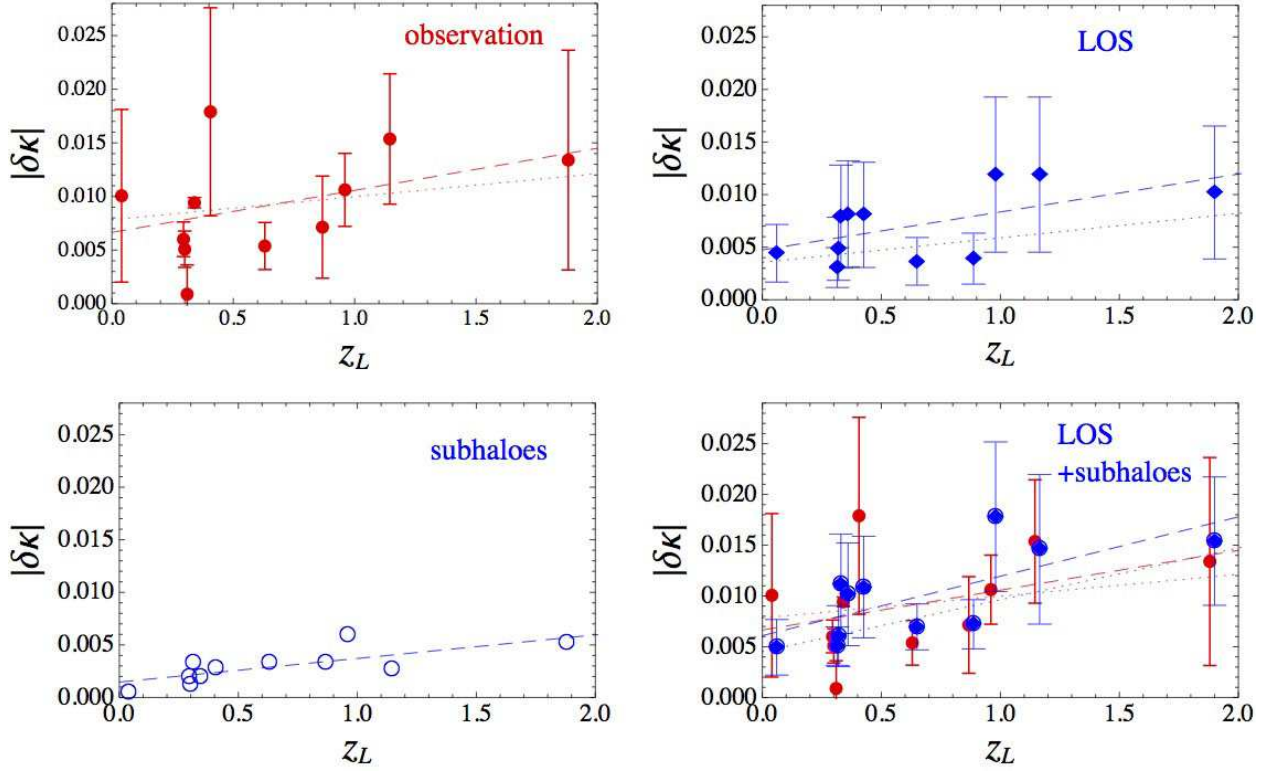


**Figure 5.** The strength of convergence perturbation  $\delta\kappa$  versus the lens redshift  $z_L$  for 11 quadruple lens samples. The parameters are the same as in figure 4.

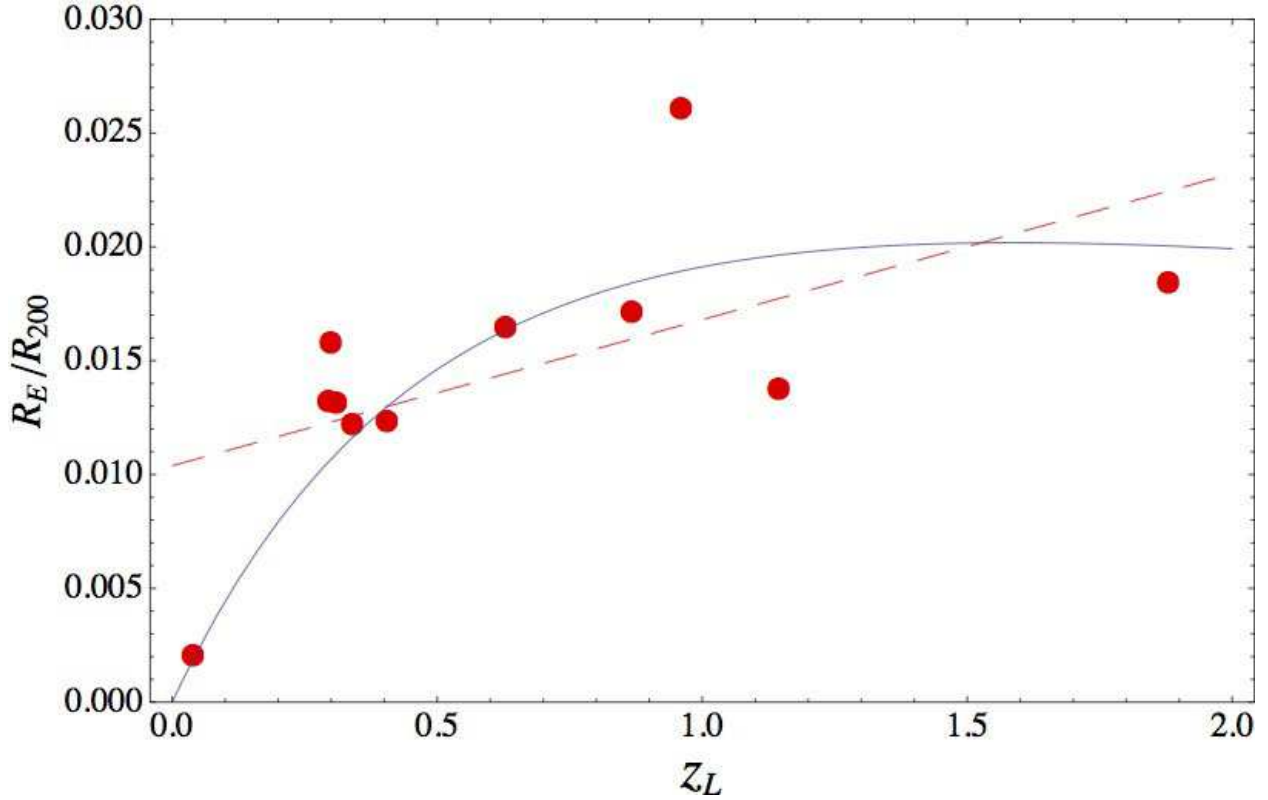


**Figure 6.** The effective Einstein radius  $R_E$  in unit of  $R_{200}$  of the lensing galaxies (red disks), the linear model fit (red dashed line), and the angular diameter distance  $D_L$  multiplied by a constant that is fitted to the data.

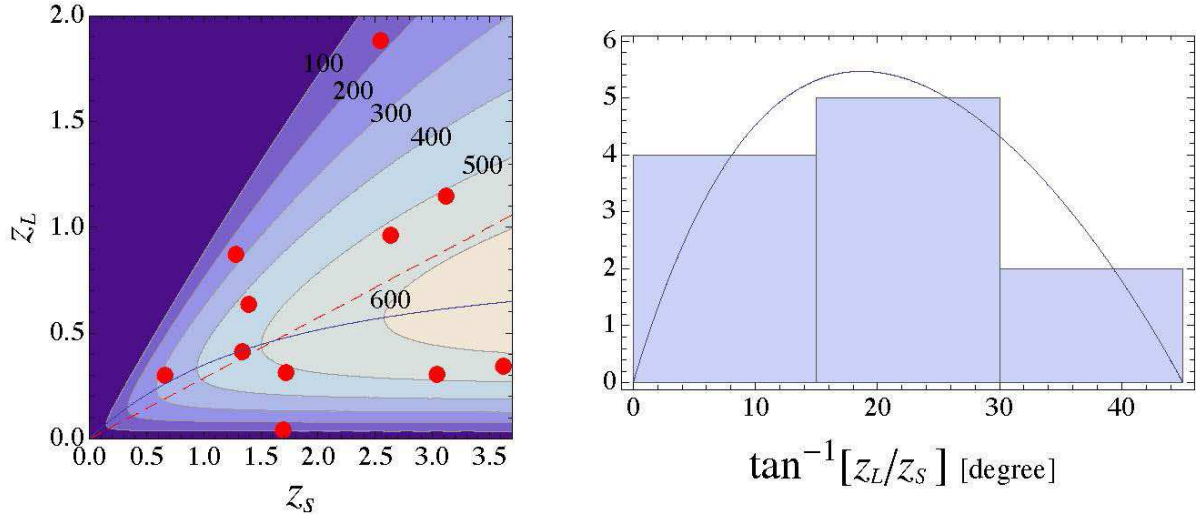


**Figure 7.** The correlation between the source redshift  $z_S$  and the lens redshift  $z_L$ . Left: the red disks are observed redshifts for 11 samples and the red dashed line shows a linear model fit without a constant basis. The boundaries of shaded regions represent contours of  $L = D_S D_L / D_{LS}$  with a decrement of  $100 h^{-1} \text{Mpc}$ . The blue curve is the ridge at which  $L$  takes its maximum for a given  $z_S$ . Right: The histogram of  $\tan^{-1}[z_L/z_S]$  of 11 samples and the distribution obtained from  $L$  integrated along  $z_L/z_S$  for  $z_S < 3.6$ .

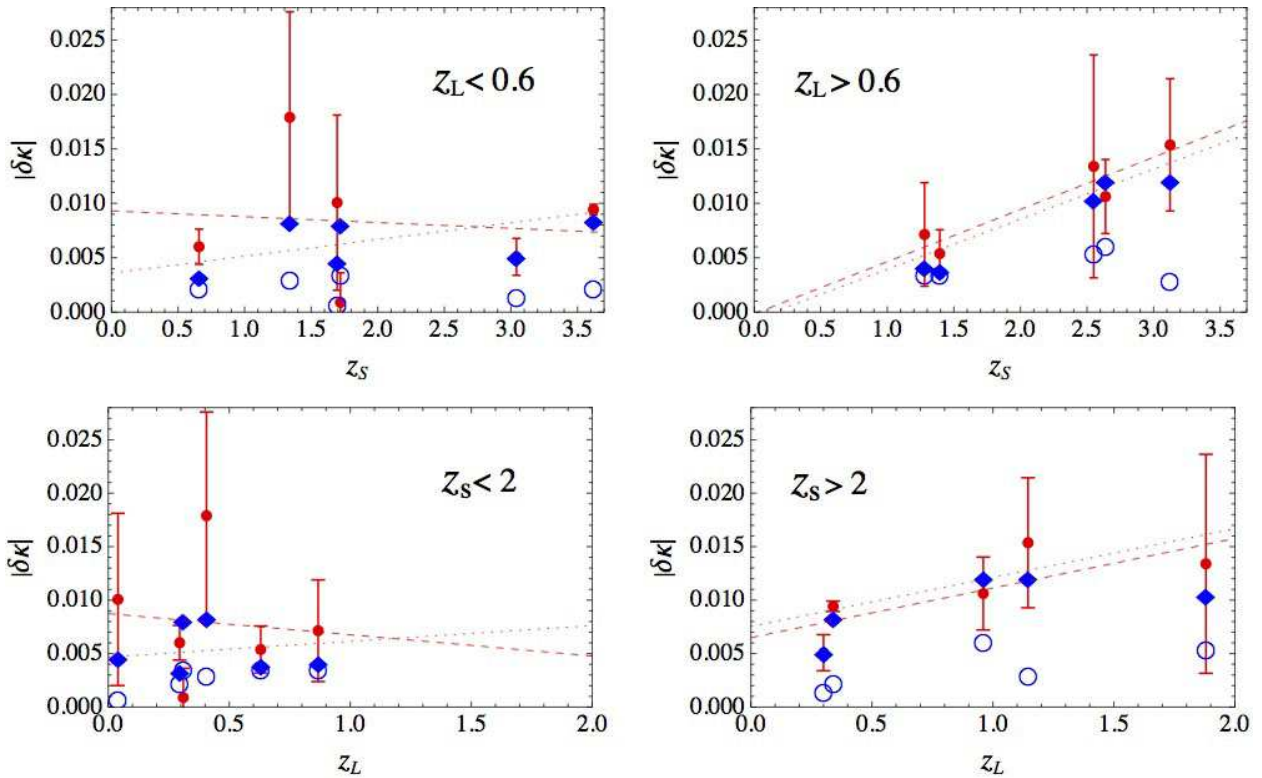


**Figure 8.** The strength of convergence perturbation  $\delta\kappa$  versus the source redshift  $z_S$  (upper) and the lens redshift  $z_L$  (lower) for 11 samples. The parameters are the same as in figure 4.

ities concern with the fluctuations of the first derivatives on scales comparable to or larger than the Einstein radius of the primary lens, we expect that our result would not be changed significantly. This is because the anomaly in the flux ratios is caused by perturbation of the second derivatives of the gravitational potential rather than the first derivatives. However, in order to obtain more accurate results, we do

need take into account these complexities as well. These issues will be addressed in our future work.

## 10 ACKNOWLEDGMENTS

The author thanks Masashi Chiba and Takeo Minezaki for valuable discussion and useful comments. This work

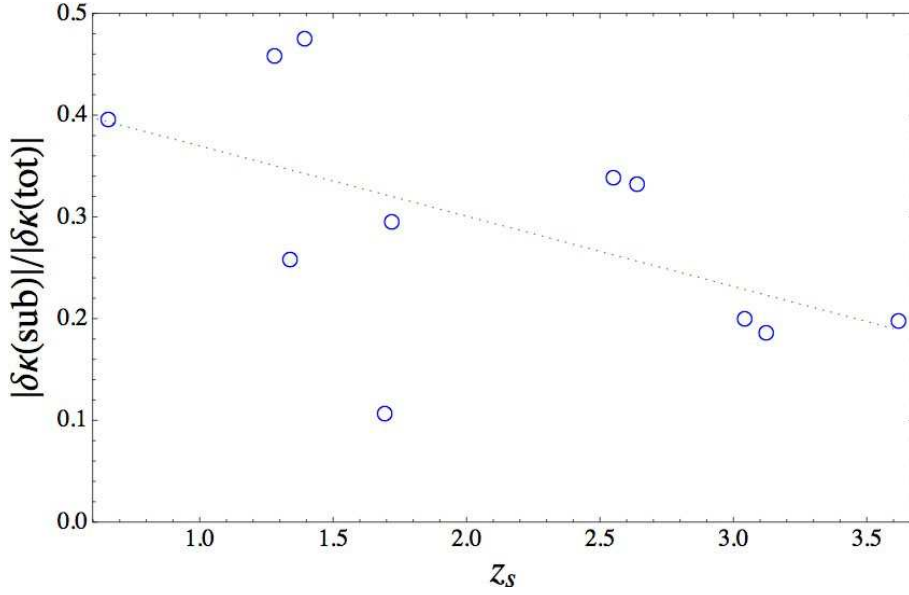


**Figure 9.** The ratio of the strength of convergence perturbation from subhaloes to that of the total (subhaloes plus line-of-sight structures) shown in blue circles and the linear model fit shown in a blue dotted line.

is supported in part by JSPS Grant-in-Aid for Scientific Research (B) (No. 25287062) “Probing the origin of primordial minihalos via gravitational lensing phenomena”. This paper makes use of the following ALMA data: ADS/JAO.ALMA#2011.0.00016.SV. ALMA is a partnership of ESO (representing its member states), NSF (USA) and NINS (Japan), together with NRC (Canada), NSC and ASIAA (Taiwan), and KASI (Republic of Korea), in cooperation with the Republic of Chile. The Joint ALMA Observatory is operated by ESO, AUI/NRAO and NAOJ.

## APPENDIX A: UNIQUENESS IN DECOMPOSITION OF STRONG+WEAK LENS

In what follows, we probe uniqueness in decomposition of a strong plus weak lens that creates a quadruple image. This proof ensures that if deflection angle caused by perturbers is too large, reparametrisation of the best-fit SIE model cannot recover the fit to all the image positions. We assume that the gravitational potential  $\Psi$  of a primary lens is sufficiently smooth and similar to that of an SIS and the lens is successfully fitted. We show that reparametrisation of dimensionless model parameters  $\mathbf{C}$  and the source angular position  $\mathbf{y}$  of the best-fitted model with  $\Psi(\mathbf{C})$  does not recover the original fit in the positions if the  $j$ -th lensed image at an angular position of  $\mathbf{x}_j$  is significantly perturbed to  $\mathbf{x}_j + \delta\mathbf{x}_j$ , where  $|\delta\mathbf{x}_j|$  far exceeds the observational error  $\varepsilon$  except for a special case in which  $\delta\mathbf{x}_j$  is parallel to the tangential arc. For brevity without loss of generality, we set the effective Einstein radius of the best-fitted model to 1 and all the  $1\sigma$  errors of observed positions of lensed images to a constant  $\varepsilon \ll 1$ .

The unperturbed lens equation for the  $i$ -th image ( $i = 1, 2, 3, 4$ ) is

$$\mathbf{y} = \mathbf{x}_i - \boldsymbol{\alpha}(\mathbf{x}_i; \mathbf{C}), \quad (\text{A1})$$

where  $\boldsymbol{\alpha}(\mathbf{x}_i; \mathbf{C})$  denotes the deflection angle obtained from  $\Psi(\mathbf{C})$ . Suppose that the  $j$ -th lensed image placed at the neighbourhood of a critical curve in the unperturbed lens is affected by a local perturber so that the position of the  $j$ -th lensed image is shifted from  $\mathbf{x}_j$  to  $\mathbf{x}'_j = \mathbf{x}_j + \delta\mathbf{x}_j$  where  $|\delta\theta_j| = \eta \gg \varepsilon$  whereas other lensed images at  $\mathbf{x}_i$ , ( $i \neq j$ ) remain the observed positions within  $\varepsilon$ . Then, we need to adjust the position  $\mathbf{x}'_j$  back to  $\mathbf{x}_j$  by changing the lens parameter  $\mathbf{C}$  to  $\mathbf{C}' = \mathbf{C} + \delta\mathbf{C}$  and the source position  $\mathbf{y}$  to  $\mathbf{y}' = \mathbf{y} + \delta\mathbf{y}$  keeping the positions of other lensed images within  $\varepsilon$ . From the perturbed lens equation and the unperturbed lens equation (A1), we have

$$\delta\mathbf{y} \approx - \left. \frac{\partial\mathbf{y}}{\partial\mathbf{x}} \right|_{\mathbf{x}_j} \delta\mathbf{x}_j - \frac{\partial\boldsymbol{\alpha}_j}{\partial\mathbf{C}} \delta\mathbf{C} \quad (\text{A2})$$

where  $\boldsymbol{\alpha}_j = \boldsymbol{\alpha}(\mathbf{x}_j; \mathbf{C})$ . Using an orthogonal transformation, the inverse magnification matrix  $\partial\mathbf{y}/\partial\mathbf{x}$  can be diagonalized as

$$\frac{\partial\mathbf{y}}{\partial\mathbf{x}} = \begin{pmatrix} 1 - \kappa - \gamma & 0 \\ 0 & 1 - \kappa + \gamma \end{pmatrix}, \quad (\text{A3})$$

where  $\kappa$  and  $\gamma$  are the convergence and shear, respectively. Assuming that the lensed images are significantly magnified and  $\Psi$  is similar to that of an SIS, we have  $\kappa = \gamma \sim 0.5$ . Then, we have

$$\frac{\partial\mathbf{y}}{\partial\mathbf{x}} \sim \begin{pmatrix} 0 & 0 \\ 0 & 1 \end{pmatrix}, \quad (\text{A4})$$

and thus the order of  $(\partial\mathbf{y}/\partial\mathbf{x})\delta\mathbf{x}_j$  is  $\eta$  except for the case in which  $\delta\mathbf{x}_j \sim (\delta x_j, 0)$ , i.e., parallel to the tangential arc. On the other hand,  $O[(\partial\mathbf{y}/\partial\mathbf{x})\delta\mathbf{x}_i] = \varepsilon$ , ( $i \neq j$ ) or smaller ( $O$  denotes order). Since

$$\left. \frac{\partial\mathbf{y}}{\partial\mathbf{x}} \right|_{\mathbf{x}_i} \delta\mathbf{x}_i + \frac{\partial\boldsymbol{\alpha}_i}{\partial\mathbf{C}} \delta\mathbf{C} = \left. \frac{\partial\mathbf{y}}{\partial\mathbf{x}} \right|_{\mathbf{x}_k} \delta\mathbf{x}_k + \frac{\partial\boldsymbol{\alpha}_k}{\partial\mathbf{C}} \delta\mathbf{C}, \quad (\text{A5})$$

for  $i \neq j$  and  $k \neq j$ , and

$$O\left[\left|\frac{\partial \alpha_i}{\partial C} \delta C\right|\right] = O\left[\frac{\alpha_i}{C} \delta C\right] = O\left[\frac{\delta C}{C}\right], \quad (\text{A6})$$

because of smoothness of  $\Psi$ , we have  $O[\delta C/C] \leq \varepsilon$  and  $O[|\delta \mathbf{y}|] \leq \varepsilon$ . However, equation (A2) and (A4) give  $O[|\delta \mathbf{y}|] = \eta$ . Thus, we cannot find any reparametrisation except for the case in which  $\delta \mathbf{x}_j$  is parallel to the tangential arc. In other words, a massive local perturber that causes a large astrometric shift makes the unperturbed model significantly differ from a smooth SIS.

## REFERENCES

- ALMA Partnership et al., 2015, *ApJ*, **808**, L4
- Barnabè M., Czoske O., Koopmans L. V. E., Treu T., Bolton A. S., 2011, *MNRAS*, **415**, 2215
- Biggs A. D., Browne I. W. A., Jackson N. J., York T., Norbury M. A., McKean J. P., Phillips P. M., 2004, *MNRAS*, **350**, 949
- Chen J., Kravtsov A. V., Keeton C. R., 2003, *ApJ*, **592**, 24
- Chen J., Rozo E., Dalal N., Taylor J. E., 2007, *ApJ*, **659**, 52
- Chiba M., 2002, *ApJ*, **565**, 17
- Chiba M., Minezaki T., Kashikawa N., Kataza H., Inoue K. T., 2005, *ApJ*, **627**, 53
- Correa C. A., Wyithe J. S. B., Schaye J., Duffy A. R., 2015, *MNRAS*, **452**, 1217
- Dalal N., Kochanek C. S., 2002, *ApJ*, **572**, 25
- Emberson J. D., Kobayashi T., Alvarez M. A., 2015, *ApJ*, **812**, 9
- Fadely R., Keeton C. R., 2012, *MNRAS*, **419**, 936
- Fassnacht C. D., Xanthopoulos E., Koopmans L. V. E., Rusin D., 2002, *ApJ*, **581**, 823
- Gao L., Navarro J. F., Frenk C. S., Jenkins A., Springel V., White S. D. M., 2012, *MNRAS*, **425**, 2169
- Han J., Cole S., Frenk C. S., Jing Y., 2016, *MNRAS*, **457**, 1208
- Hsieh J.-W., Fassnacht C. D., Vegetti S., McKean J. P., Spingola C., Auger M. W., Koopmans L. V. E., Lagattuta D. J., 2016, preprint, ([arXiv:1601.01671](https://arxiv.org/abs/1601.01671))
- Humphrey P. J., Buote D. A., 2010, *MNRAS*, **403**, 2143
- Inoue K. T., Chiba M., 2003, *ApJ*, **591**, L83
- Inoue K. T., Chiba M., 2005a, *ApJ*, **633**, 23
- Inoue K. T., Chiba M., 2005b, *ApJ*, **634**, 77
- Inoue K. T., Takahashi R., 2012, *MNRAS*, **426**, 2978
- Inoue K. T., Takahashi R., Takahashi T., Ishiyama T., 2015, *MNRAS*, **448**, 2704
- Inoue K. T., Minezaki T., Matsushita S., Chiba M., 2016, *MNRAS*, **457**, 2936
- Keeton C. R., Moustakas L. A., 2009, *ApJ*, **699**, 1720
- Keeton C. R., Gaudi B. S., Petters A. O., 2003, *ApJ*, **598**, 138
- Kochanek C. S., Dalal N., 2004, *ApJ*, **610**, 69
- Koopmans L. V. E., 2005, *MNRAS*, **363**, 1136
- Koopmans L. V. E., et al., 2003, *ApJ*, **595**, 712
- Koopmans L. V. E., et al., 2009, *ApJ*, **703**, L51
- Kormann R., Schneider P., Bartelmann M., 1994, *Astronomy and Astrophysics*, **284**, 285
- Lagattuta D. J., Auger M. W., Fassnacht C. D., 2010, *ApJ*, **716**, L185
- MacLeod C. L., Kochanek C. S., Agol E., 2009, *ApJ*, **699**, 1578
- MacLeod C. L., Jones R., Agol E., Kochanek C. S., 2013, *ApJ*, **773**, 35
- Mao S., Schneider P., 1998, *MNRAS*, **295**, 587
- McKean J. P., et al., 2007, *MNRAS*, **378**, 109
- Metcalf R. B., 2005, *ApJ*, **629**, 673
- Metcalf R. B., Madau P., 2001, *ApJ*, **563**, 9
- Metcalf R. B., Moustakas L. A., Bunker A. J., Parry I. R., 2004, *ApJ*, **607**, 43
- Minezaki T., Chiba M., Kashikawa N., Inoue K. T., Kataza H., 2009, *ApJ*, **697**, 610
- More A., McKean J. P., More S., Porcas R. W., Koopmans L. V. E., Garrett M. A., 2009, *MNRAS*, **394**, 174
- Oguri M., Rusu C. E., Falco E. E., 2014, *MNRAS*, **439**, 2494
- Planck Collaboration et al., 2014, *Astronomy and Astrophysics*, **571**, A1
- Sluse D., Chantry V., Magain P., Courbin F., Meylan G., 2012, *Astronomy and Astrophysics*, **538**, A99
- Springel V., et al., 2008, *MNRAS*, **391**, 1685
- Sugai H., Kawai A., Shimono A., Hattori T., Kosugi G., Kashikawa N., Inoue K. T., Chiba M., 2007, *ApJ*, **660**, 1016
- Takahashi R., Inoue K. T., 2014, *MNRAS*, **440**, 870
- Vegetti S., Lagattuta D. J., McKean J. P., Auger M. W., Fassnacht C. D., Koopmans L. V. E., 2012, *Nature*, **481**, 341
- Vegetti S., Koopmans L. V. E., Auger M. W., Treu T., Bolton A. S., 2014, *MNRAS*, **442**, 2017
- Xu D. D., et al., 2009, *MNRAS*, **398**, 1235
- Xu D. D., Mao S., Cooper A. P., Wang J., Gao L., Frenk C. S., Springel V., 2010, *MNRAS*, **408**, 1721
- Xu D. D., Mao S., Cooper A. P., Gao L., Frenk C. S., Angulo R. E., Helly J., 2012, *MNRAS*, **421**, 2553
- Xu D., Sluse D., Gao L., Wang J., Frenk C., Mao S., Schneider P., Springel V., 2015, *MNRAS*, **447**, 3189
- van den Bosch F. C., Tormen G., Giocoli C., 2005, *MNRAS*, **359**, 1029